EFFECT OF IN-PLANE INDUCED VELOCITIES ON THE STEADY STATE MODELLING OF A HELICOPTER USING A TIME MARCHING WAKE

Maria Ribera Vicent

4 Everlands Close, Woking, Surrey GU22 7B, UK
+44 07884 452400, mariaribera@gmail.com

ABSTRACT

The effect of an accurate prediction of the induced velocities on the steady state flight solution of a helicopter was investigated with a flight dynamics model coupled with a time-marching free wake. In particular, the radial and tangential induced velocities, often neglected, were added to the model. The results were obtained for a range of speeds and turn rates and validated against flight test data. The radial induced velocity was found to be very small, except for the regions where the vortex filaments were very close to the rotor. The tangential induced velocity, on the other hand, was more significant in magnitude and its effect on the angle of attack and aerodynamic loads was described. In general, the tangential induced velocity was found to lower the angle of attack over much of the rotor, except for on the rear retreating side where it had the opposite effect. The trim results showed that a similar trend is obtained with both models, however including all induced velocities produces slightly higher power and collective requirements, but similar or moderately lower values for the helicopter orientation and cyclic controls. It was also found that the effects of the in-plane induced velocities on turning flight were not symmetrical, with slightly different predictions on left and right turns.

1. NOMENCLATURE

C_D	Drag coefficient
C_L	Lift coefficient
$rC_DM^2\cos\phi$	Elemental profile torque
$rC_LM^2\sin\phi$	Elemental induced torque
D_ψ	Finite difference approximation to the time derivative
D_ζ	Finite difference approximation to the spatial derivative
$I_{b_{i,j}}$	Bound influence coefficient matrix
$I_{NW_{i,j}}$	Near wake influence coefficient matrix
M	Mach number
N_S	Number of blade segments
p, q, r	Roll, pitch and yaw rates of the helicopter, deg/sec
$q_0^k, q_{nc}^k, q_{ns}^k$	Constant and harmonic coefficients of the k^{th} blade mode
r	Blade radial station, ft
$\mathbf{r}$	Position vector of a point on the filament
t	time, sec
u, v, w	Velocity components on body axes, ft/sec
$\mathbf{u}$	Vector of controls
U_T, U_R, I_P	Tangential, radial and perpendicular blade sectional velocities
V	Helicopter velocity along the trajectory
$\mathbf{V}(\mathbf{r})$	Total velocity at a point $\mathbf{r}$ on the filament
V_x, V_y, V_z	Blade velocities
V_∞	Stream velocity at the control points
$\mathbf{X}$	Vector of trim unknowns
$\mathbf{y}$	Vector of states
$\dot{\mathbf{y}}$	Vector of state derivatives
α_F, β_F	Fuselage angle of attack and sideslip angle, deg
$\beta(\psi)$	Flap angle; flap distribution, deg
Γ	Circulation
$\Delta\psi$	Wake azimuth resolution, deg
$\Delta\zeta$	Vortex filament discretization resolution, deg
ζ	Age of the vortex filament, deg
θ_F	Fuselage pitch attitude, deg
θ	Geometric angle of attack, deg
λ_{0t}	Tail rotor inflow coefficient
$\lambda_x, \lambda_y, \lambda_z$	Induced velocity coefficients
ϕ_F	Bank angle, deg
ϕ_{FW}	Induced angle of attack due to the far wake, deg
ψ	Blade azimuth angle, deg
Ω	Rotor speed, rad/sec

Abbreviations

ODE	Ordinary Differential Equation
PC2B	Predictor-Corrector 2^{nd}-order Backward difference

2. INTRODUCTION

As the requirements for faster, greener, quieter and more efficient helicopters increase, so does the need for more sophisticated models that provide accurate predictions in a variety of practical problems of helicopter aeromechanics. It is important to make sure that those models can be relied on to capture a wide range of flight conditions, such as the response to pilot inputs in moderate and large amplitude unsteady manoeuvres, turning and descending flight.

There are nowadays a number of rotorcraft models to choose from, each with their own strengths and weaknesses. Building a comprehensive simulation model involves the coupling of many sub-systems, such as the aeroelastic rotor, the rotor wake, the fuselage, etc, which are not independent of each other and interact between themselves, adding another level of complexity to the behaviour of the helicopter model. Many rely on dynamic inflow models[1], gaining computational speed and simplicity, but losing the full understanding of the wake dynamics. Other models have more advance rotor/body aerodynamics[2], but with simpler structural blade models. However, there is a significant effort being made towards comprehensive models that combine the state of the art in aerodynamics and structural dynamics.

The study on which the present work is based[3,4,5] describes the formulation and validation of such a simulation model, in which a finite element based rotor model and large amplitude fuselage dynamic equations are coupled with a free wake model capable of capturing correctly the wake geometry distortions. This model can describe steady state flight conditions, both in straight, descending and turning flight, and the free flight response to pilot inputs, with no restriction on the amplitude of the inputs or of the helicopter response.

One of the general assumptions made in the studies that form the base of this work[3,6] is that, while the wake model provides all three spatial components of the induced velocities, the x and y components, radial outward and in the lead direction respectively, are set to zero, and only the z component is used for the calculation of the aerodynamic loads. It was assumed that the x and y components are negligible in comparison with the z component. This assumption is quite common in helicopter models, even in those of some complexity.

There has been some effort into looking at the tangential component in the modelling of horizontal axis wind turbines, as it is of higher significance for wind turbines than it is for helicopter rotors. Even some work has been done to look at the effect of the radial component, which even in wind turbine models is usually neglected[7]. But little reference to the induced velocities in the x and y direction is made in rotorcraft models.

Some of the results in the work that form the base for this study[3] gave an indication that perhaps, in some flight conditions, these in-plane induced velocities might not be as small as previously considered, and perhaps not negligible, as previously supposed. In particular, some descents[4], in which the wake vortex filaments get closer to the rotor, and even cross the rotor plane, and some manoeuvres, such as the descent into the vortex ring state[5], in which the bundled vortex filaments approach the rotor until a vortex ring is formed.

This paper removes this assumption. The asymmetry of the in-plane induced velocities is expected to have some effect on the aerodynamic loads and therefore on the overall rotor and helicopter attitude and rates.

The specific objectives of this paper are

1. To describe the coupling of the free wake model with the rotor and fuselage models for trim calculations;
2. To present the results of trim at various flight conditions (level, turning flight) with the inclusion of the x and y induced velocity components, and analyse their effect on the aerodynamic loads and helicopter behaviour;
3. To provide some validation with flight test data when such data is available.

3. MATHEMATICAL MODEL

3.1. Rotor and fuselage dynamics

The flight dynamics model used in the present study [3,4,5] is based on a system of coupled nonlinear rotor-fuselage differential equations in first-order, state-space form. It models the rigid body dynamics of the helicopter with the non-linear Euler equations. The aerodynamic characteristics of the fuselage and empennage are included in the form of look-up tables. The dynamics of the rotor blades are modelled with coupled flap, lag and torsion, a finite element discretisation and a modal coordinate transformation to reduce the number of degrees of freedom. There is no limitation on the magnitudes of the hub motions. In particular, the effects of large rigid body motions on the structural, inertia, and aerodynamic loads acting on the flexible blades are rigorously taken into account.

The resultant of combining the rotor blade equations and the fuselage equations is a set of ODEs, which can be formulated explicitly, in the form

$$\dot{\mathbf{y}} = \mathbf{f}(\mathbf{y}, \mathbf{u}; \mathbf{t}) \tag{1}$$

or implicitly, in the form

$$\mathbf{f}(\dot{\mathbf{y}}, \mathbf{y}, \mathbf{u}; \mathbf{t}) = \mathbf{0} \tag{2}$$

where $\mathbf{y}$ is the vector of states, $\dot{\mathbf{y}}$ is the vector of state derivatives and $\mathbf{u}$ is the vector of controls. The vector of states contains the three body velocities and rates, the three Euler angles and the rotor states. The tail rotor inflow is modelled with one-state dynamic inflow.

3.2. Wake model

Free wake methods model the rotor flow field using vortex filaments that are released at the tip of the blade. A schematic of the wake discretisation is shown in Figure 17. The distortions of the wake geometry due to manoeuvres are taken into account without *a priori* assumptions on the geometry.

The behaviour of the vortex filaments is described by a convection equation of the form

$$\frac{\partial \mathbf{r}(\psi,\zeta)}{\partial \psi} + \frac{\partial \mathbf{r}(\psi,\zeta)}{\partial \zeta} = \frac{1}{\Omega}\mathbf{V}(\mathbf{r}(\psi,\zeta)) \tag{3}$$

where $\mathbf{r}(\psi,\zeta)$ is the position of a point on the vortex filament and $\mathbf{V}(\mathbf{r}(\psi,\zeta))$ is the local velocity at that given point. The wake geometry is discretised in two domains, ψ and ζ. The first represents the time component and is obtained by dividing the rotor azimuth domain into a number of angular steps of size $\Delta\psi$. The second represents the age of the vortex filament, which is discretised into a number of straight line vortex segments of size $\Delta\zeta$. The right hand side of Eq. (3) is formed of the addition of the free stream velocity, the velocities induced by all the other vortex filaments and the blades, plus other external velocities such as those due to manoeuvring. The induced velocity is the most complicated and expensive term to compute, and Biot-Savart law is used to calculate the induced contribution of each vortex segment at any point in the wake.

The discretisation of the left hand side of Eq. (3) and its solution depend upon the type of free wake model used. In this study, the free wake model used is the Bhagwat and Leishman free wake[8,9], which is a time-accurate free wake model with a five-point central difference scheme to describe the spatial derivative, D_ζ, given by

$$\begin{aligned} D_\zeta \approx \frac{\partial \mathbf{r}(\psi+\Delta\psi/2, \zeta+\Delta\zeta/2)}{\partial\psi} = \\ \frac{[\mathbf{r}(\psi+\Delta\psi,\zeta+\Delta\zeta) - \mathbf{r}(\psi,\zeta+\Delta\zeta)]}{2\Delta\psi} + \\ + \frac{[\mathbf{r}(\psi+\Delta\psi,\zeta) - \mathbf{r}(\psi,\zeta)]}{2\Delta\psi} \end{aligned} \tag{4}$$

and a predictor-corrector with second order backward (PC2B) scheme for the time derivative, D_ψ:

$$\begin{aligned} D_\psi \approx \frac{\partial \mathbf{r}(\psi+\Delta\psi/2,\zeta)}{\partial\psi} = \\ \frac{3\mathbf{r}(\psi+\Delta\psi,\zeta) - \mathbf{r}(\psi,\zeta) - 3\mathbf{r}(\psi-\Delta\psi,\zeta)}{4\Delta\psi} \\ \frac{-\mathbf{r}(\psi-2\Delta\psi,\zeta)}{4\Delta\psi} \end{aligned} \tag{5}$$

This method is not restricted by the flight condition. Since time marching methods do not have to enforce any boundary condition, they can be used for transient conditions in which periodicity can not be enforced, and therefore relaxation methods can not be used rigorously.

The bound circulation is obtained using a Weissinger-L lifting surface model, which discretises the wake into N_S segments. A control point is located at 3/4 of the chord of each segment, while the bound circulation is at the quarter-chord location, and assumed constant along the segment. The difference in circulation between consecutive segments is trailed behind the blade at segment endpoints, with a vortex strength equal to the difference between the two segments bound vortex strengths. The near wake is comprised of these trailed vortices. The tip vortex that constitutes the free wake extends beyond the near wake with a strength equal to the maximum bound circulation along the blade. The governing equation for the Weissinger-L method is written as

$$\sum_{j=1}^{N_S} \left[I_{b_{i,j}} + I_{NW_{i,j}}\right] \Gamma_j = V_{\infty_i}(\theta_i - \phi_{FW_i}) \tag{6}$$

with i going from 1 to N_S. $I_{b_{i,j}}$ and $I_{NW_{i,j}}$ are the bound and near wake influence coefficient matrices, respectively. The stream velocities at the control point, V_∞, are calculated by the flight dynamics model. They include the velocity due to the translation and rotation of the helicopter, the velocity due to the blade motion and flexibility and the induced velocities.

3.3.The trim solution

A coordinated steady helical turn is determined by the velocity V, the flight path angle γ and the rate of turn $\dot{\psi}$. Straight and level flight is a particular case in which both the flight path angle and the rate of turn are zero. Similarly, $\dot{\psi}$ is nonzero for turns and γ is nonzero for climbing and descending flight.

The trim equations are a system of nonlinear algebraic equations, which include: 3 force equilibrium equations, 3 moment equilibrium equations, 3 kinematic equations relating the rate of turn to the body angular velocities, a turn coordination equation, an expression for the flight path angle, any inflow equations if inflow described with a state-space model

such as dynamic inflow (none in our case, as inflow is provided by free wake, solved separately), an equation for the tail rotor inflow, and the rotor equations (number depends on how many modes are retained in modal coordinate transformation and the number of harmonics used for each mode).

The trim unknowns are:

$$\begin{aligned}\mathbf{X} &= [\theta_0\ \theta_{1c}\ \theta_{1s}\ \theta_{0t}\ \alpha_F\ \beta_F\ \theta_F\ \phi_F\ \lambda_t \dots \\ &\quad \dots q_0^1\ q_{1c}^1\ q_{1s}^1\ q_{2c}^1\ q_{2s}^1 \dots q_{N_{\mathrm{h}}c}^1\ q_{N_{\mathrm{h}}s}^1 \dots \\ &\quad \dots q_0^{N_{\mathrm{m}}}\ q_{1c}^{N_{\mathrm{m}}}\ q_{1s}^{N_{\mathrm{m}}}\ q_{2c}^{N_{\mathrm{m}}}\ q_{2s}^{N_{\mathrm{m}}} \dots q_{N_{\mathrm{h}}c}^{N_{\mathrm{m}}}\ q_{N_{\mathrm{h}}s}^{N_{\mathrm{m}}}]^\top \end{aligned} \tag{7}$$

where $\theta_0, \theta_{1c}, \theta_{1s}$ and θ_{0t} are the collective, cyclic and tail pitch, respectively, $\alpha_F, \beta_F, \theta_F$ and ϕ_F are angle of attack, sideslip, pitch angle and bank angle of the fuselage, λ_t is the dynamic inflow coefficient for the tail rotor, and the q_x^k terms are the constant and harmonic coefficients of the k^{th} blade mode.

The trim solution to the system of rotor-fuselage equations is obtained with a nonlinear algebraic equation solver, using a modified Powell hybrid method[10]. It builds a Jacobian matrix by a forward difference approach, and then finds a better approximation to the solution by iterating the trim vector.

3.4.Coupling of free wake and rotor-fuselage models

The time marching free wake model cannot be solved alongside the rest of the trim equations. Not only it is not expressed in state-space form, but also it is subject to numerical instabilities and must use its own solution method. For those reasons, the free wake model is solved separately at each step of the trim iteration to provide the main rotor induced velocities. For each guess of the trim solution, the velocities seen by the blade due to the helicopter translation and rotation, blade motion and blade flexibility, $V_x(\psi, r), V_y(\psi, r), V_z(\psi, r)$, are calculated, as well as the equivalent flapping angles, $\beta(\psi)$. Together with the body rates and velocities, u, v, w, p, q, they are passed to the free wake model, which adds the induced velocities to the blade velocities in order to calculate the circulation distribution with a Weissinger-L method. With this circulation, the free wake iteration starts, determines the geometry and the corresponding induced velocities, and then updates the circulation distribution for these. The process is then repeated until the inflow converges. This method allows for much faster convergence than that in the previous approach[6], with cost savings of more than an order of magnitude.

The free wake model returns the inflow distribution for that particular flight condition, $\lambda_x(\psi, r)$, $\lambda_y(\psi, r)$ and $\lambda_z(\psi, r)$.

The velocities $V_x(\psi, r), V_y(\psi, r)$ and $V_z(\psi, r)$ are the components of the total velocity at the blade. When the inflow is converged for each step of the nonlinear equation solver and returned to the flight dynamics model, the total velocity of the air at each point in the blade can be calculated. In previous studies with this model, only the vertical component of the induced velocity, in the z direction, was considered, and the λ_x and λ_y were set to zero. But the point of this study is to include both components in the rotor plane and observe their effect on the overall aerodynamics. Therefore, the velocity at any given point with the induced velocities becomes:

$$\begin{aligned}\mathbf{V}_T &= (V_x + \lambda_x)\hat{\mathbf{e}}_x + (V_y + \lambda_y)\hat{\mathbf{e}}_y + \\ &\quad (V_z + \lambda_z)\hat{\mathbf{e}}_z\end{aligned} \tag{8}$$

The above velocities can also be expressed in the blade sectional aerodynamics coordinate system,

$$\mathbf{V}_A = U_T\mathbf{e}_T + U_P\mathbf{e}_P + U_R\mathbf{e}_R \tag{9}$$

where $\mathbf{e}_T$ points in the lag direction, $\mathbf{e}_R$ is tangent to the elastic axis and points outwards and $\mathbf{e}_P$ is positive upwards.

The sectional aerodynamic angle of attack, α,can be expressed as

$$\alpha = \theta - \phi = \theta - \frac{U_P}{U_T} \tag{10}$$

An increase in λ_z would decrease the perpendicular component of the airflow at the section, U_P, and therefore increase the angle of attack. And an increase in λ_y would decrease the angle of attack.

4. RESULTS

The results shown in this study have been obtained for a helicopter similar to the UH-60, at 16,000 lbs and an altitude of 5250 ft. The flexible blade is modelled with 4 finite elements, and 5 blade modes are retained in the modal coordinate transformation (2 flap, 2 lag and 1 torsion). The free wake has been modelled with 4 free turns downstream of the rotor. A 10^o discretisation is used for both the time and space derivatives. Trim conditions has been obtained between the speeds of 1k (illustrative of hover) and 140 its in level flight, and for rates of turn between $\dot{\psi} = -20$ and $\dot{\psi} = 20$ deg/sec at a speed of 60 kts.

4.1. Straight and level flight

Figure 1 shows the x, y and z components of the induced velocities at speeds of 1 kt, 60 kts and 140 kts. In near hover conditions, all velocities are nearly axisymmetric, with a ring-like appearance. The radial and tangential components have nearly zero values for the inner part of the rotor but concentric rings of

higher positive and negative values near the tips, due to the proximity of the vortex filament. The perpendicular component, the traditional inflow, is high all over the rotor, with a slight bias to the front, as all the wake vortices are concentrated below the rotor and exerting their influence quasi axi-symmetrically. As the speed increases, the wake begins to skew, and the vortices interact between themselves as their proximity increases. At 60 kts, the radial velocity is close to zero over most of the rotor, but some arched bands of higher values in the front of the rotor reveal the influence of the front wake filaments that are starting to be washed backwards at this speed. The y component shows some of these axisymmetric bands in the front half, but in lesser magnitude. The interesting behaviour occurs in the back half of the rotor. On the advancing side, there is a large region of negative λ_y, while on the fourth quarter a large area of positive values of λ_y can be seen. The perpendicular component λ_z shows the area of higher influence has shifted to the rear half of the rotor, as the wake is trailed behind, and the front half has nearly zero values at this speed. At 140 kts, the wake is pushed farther back and the influence of the wake filaments on λ_x is reduced. At this speed, λ_x is nearly zero over most of the rotor. λ_y is slightly lower in the rear retreating side, but on the advancing side still presents an area of large negative values. λ_z has a region of upwash in the front of the rotor, and the values in the rear half of the rotor continue to decrease as the wake filaments are stretched very far behind.

From Equation 10, it follows that an increase in the perpendicular induced velocity will produce a decrease in the angle of attack, while an increase in the tangential component will produce a higher angle of attack. Figure 2 depicts the angle of attack at speeds of 1 kt, 60 kts and 140 kts, both when only the λ_z is included as when λ_x and λ_y are considered as well. In hover, the differences are very small, as both in-plane induced velocities are nearly zero, and the angle of attack is almost uniform with a small variation between 3 and 5 degrees. At 60 kts, the lower perpendicular induced velocities at the front of the rotor translate into higher angle of attack in that region, while the areas in the retreating and rear sides of the rotor, where λ_z is higher, show values of lower α. However, the relationship is not direct, as now we can account for the effect of λ_y. On the first and third quadrants of the rotor, the low negative values of the tangential induced velocity reduce the angle of attack, which is lower there in the case when all the induced velocities are included than when not, while in the fourth quadrant the opposite is true, but in lesser magnitude. At high speeds, a similar effect is observed, a large region of low values of λ_y on the advancing side reduce the overall angle of attack, while at the retreating side it is nearly zero and has very little effect on α.

The lift and drag coefficients, C_L and C_D, are a function of angle of attack and Mach number, and since the Mach number is also a function of the tangential velocity, both coefficients will be affected by the inclusion of λ_y.This relationship is not straightforward to deduce, but the following are observations on the comparison between the cases when the in-plane induced velocities are included and when they are assumed zero. For brevity, we will consider only the case when 60 kts. Figure 3 shows the lift and drag coefficients, C_L and C_D, as well as the elemental induced torque, $rC_LM^2 \sin\phi$, and elemental profile torque, $rC_DM^2 \cos\phi$, with and without in-plane induced velocities, at 60 kts. The lift coefficient, C_L, is slightly higher when $\lambda_x = \lambda_y = 0$, as is the angle of attack, specially on the retreating side. The elemental induced torque, $rC_LM^2 \sin\phi$, shows a region of slightly negative values in the front of the rotor, although mostly the contribution to power occurs in the rear half of the rotor. Including the in-plane induced velocities seems to produce higher induced torque at this speed. The drag coefficient C_D shows large areas where it takes a value around 0.008, however there are three regions where the drag reaches considerably larger values: first, near the tip on the advancing side, where the Mach number is highest, then the region in the outer third quadrant, where the vortex filaments have a strong effect on all three induced velocity components, and therefore on the angle of attack, and at the rear of the rotor plane. Including the tangential induced velocity seems to lower the drag, particularly in the third quadrant. The elemental profile torque, $rC_DM^2 \cos\phi$, is low over most of the rotor, but increases radially towards the tip, and is maximum at the tip on the advancing side. While very similar, it appears moderately higher when λ_x and λ_y are computed into the total velocities.

So far, little has been said of the radial induced velocities, as it has not produced a direct effect on the variables described. However, the overall speed $\mathbf{V}_T$ at each blade station, which is the sum of all three velocities, will be affected by any variations in the radial induced velocity. The total velocity is needed for the computation of the total forces and moments, and therefore thrust and power. From Figure 1, we can gather that this effect will indeed be very small, as λ_x is very low, except for a few bands when the vortex filaments are close. So in general, the effect of λ_x is insignificant, unless one needs to have a very accurate prediction of the velocity and aerodynamic loads locally in the regions of close proximity with the vortex filaments.

The overall power required as a function of speed is shown in Figure 4. Including the in-plane induced velocities, the model predicts slightly higher power requirement at high speeds, although in low to transition

speeds the predicted power is lower. From the analysis of the elemental induced torque and elemental profile torque at 60 kts from Figure 3, we can see that the induced torque is slightly higher, while the profile torque is starting to become more significant as the tip speeds on the advancing side produce high drag.

Figure 5 shows the helicopter pitch attitude as a function of speed, both with the in-plane velocities considered and forced to zero, along with the available flight test data. These results show that at lower speed both models have a very similar behaviour and both overestimate the flight test data. This over prediction can be attributed to the lack of a rotor/fuselage aerodynamic interaction model. At higher speeds, both models capture the trend correctly, with the model including all induced velocities predicting slightly lower pitch attitude at higher speeds.

Figure 6 shows the bank angle as a function of speed, again comparing the effect of λ_x and λ_y as well as flight test data. In this case, both models underestimate the bank angle at high speeds in a similar manner. At low speed, however, the trend of flight test data is captured accurately. The effect of including all induced velocities is to trim at slightly lower bank angles.

Figure 7 shows the main rotor collective stick as a function of speed, which behaves in a similar manner as the power required.

The cyclic controls, longitudinal and lateral stick, are shown in figures 8 and 9. The longitudinal stick is underestimated at low speed, possibly due to the lack of rotor downwash-fuselage interaction in the model, but correctly captured at higher speeds. The model with in-plane induced velocities predicts slightly lower values of the longitudinal stick position. The lateral stick is captured by both models with good agreement, with slightly higher values attained when λ_x and λ_y are not zero.

4.2. Turning flight

The induced velocities for turning flight at rates of turn of -20 deg/sec and 20 deg/sec are shown in Figure 10. As in straight and level flight, the radial induced velocity shows values close to zero for great parts of the rotor, except in those areas where the vortex filaments are close, where the bands of high λ_x closely follow the shape of the vortices below. Both left and right turn are very similar. The tangential induced velocity also looks similar to the straight and level values at the same speed, in Figure 1, with low negative values in the first and third quadrant and high positive values in the fourth. However, as the helicopter turns the wake bends into itself and the proximity of the vortex filaments increases. The magnitude of their influence at the rotor level increases, producing even more negative values on the advancing side and higher values on the retreating side. This seems to be slightly more pronounced in the left turn, at $\dot{\psi} = -20$deg/sec, than in the equivalent right turn. The perpendicular induced velocity is nearly zero in the front half of the rotor, with a slight upwash flow, but higher at the rear of the rotor than in level flight, as the wake is closer and its influence greater. The right turn seems to show values of λ_z moderately larger than the left turn.

Figure 11 shows the angle of attack at $\dot{\psi} = -20$ deg/sec and $\dot{\psi} = 20$ deg/sec, both with the perpendicular induced velocity only and with all induced velocities considered. The lower values of λ_y on the advancing and front sides of the rotor decrease the magnitude of the angle of attack, and on the rear retreating side λ_y has a positive contribution to α. In comparison, the angle of attack on the right turn appears moderately larger than on the left turn.

The power required in turning flight at 60 kts for a range of bank angles, predicted by both models, is shown in Figure 12. Both models capture the trend of flight test data results correctly. Including all induced velocities produces slightly higher power requirements throughout the range of roll angles. The main rotor collective, shown in Figure 15, shows a similar behaviour.

Figure 13 shows the pitch attitude as a function of roll angle at 60 kts. While both models over predict the flight test data values, the trend is better captured on the left turns. The inclusion of all the induced velocities in the model helps improve the prediction of the left turns, while on the right turns it produces higher results than without λ_x and λ_y.

The longitudinal control as a function of roll angle at 60 kts is shown in Figure 14, does not capture the trend at all, in fact moving in the opposite direction of the flight test data.

Finally, the main rotor lateral stick displacement is shown in Figure 16, for a range of roll angles at 60 kts. Both models capture the experimental results accurately, and the prediction is similar for both left and right turns. The results with nonzero λ_x and λ_y are slightly higher, mostly at the higher roll angles, both in left and right turns.

6. CONCLUSIONS AND FUTURE WORK

This paper set out to study the effect of including all three components of the induced velocities, radial, tangential and perpendicular, on the steady state solution of a helicopter, using a comprehensive flight mechanics model with refined aerodynamics provided by the Bhagwat-Leishman free wake model. The purpose of the exercise is, in part, to explain the relationship between the wake dynamics and the velocities it

induces at the rotor plane with the behaviour of the helicopter. The other purpose is to lay the basis for an analysis of manoeuvring flight.

The main conclusions obtained from the present study are:

1. The radial induced velocity is in general very small, although locally it can reach high values where the vortices are in close proximity. Its effects are difficult to trace but important whenever an accurate knowledge of the elemental velocities is needed.
2. The tangential induced velocity has a moderate but visible effect on the angle of attack, as well as on the Mach number, and its effect can clearly be traced on the aerodynamic coefficients and overall rotor loads.
3. The effect of the in-plane induced velocities is different on left and right turns.
4. The prediction of power requirements, rotor controls and helicopter orientation are slightly different but similar enough that the assumption of $\lambda_x = \lambda_y = 0$ can be made safely for most purposes. However, for studies in which an accurate knowledge of the rotor loads and localised velocities is needed, it is recommended to include the in-plane induced velocities, particularly λ_y.

Though it has not been done due to size limitations, it is recommended for the future to explore the effect of the in-plane induced velocities on the blade dynamics, in particular the effect of the drag obtained with tangential induced velocities on the lag motion.

The logical continuation of this project consists on analysing the effects of all the induced velocities in descending and manoeuvring flight. The increased proximity of the vortex filaments, not just in steady descents but also in other transient manoeuvres that bring the wake into closer interaction with the rotor, is expected to have some more significant contribution than in steady level and turning flight.

6. COPYRIGHT STATEMENT

References

[1] Peters, D. A., and He, C. J., "Correlation of Measured Induced Velocities with a Finite-State Wake Model," *Journal of the American Helicopter Society*, Vol. 36, No. 3, July 1991, pp. 59–70.

[2] Brown, R. E., Line, A. J., and Ahlin, G. A., "Fuselage and Tail-Rotor Interference Effects on Helicopter Wake Development in Descending Flight," Proceedings of the 60^{th} Annual Forum of the American Helicopter Society International, 2004.

[3] Ribera, M., *Helicopter Flight Dynamics Simulation With a Time-Accurate Free-Vortex Wake Model* PhD thesis, University of Maryland, 2007.

[4] Ribera, M., and Celi, R., "Simulation Modeling in Climbing and Descending Flight with Refined Aerodynamics," Proceedings of the 62nd Annual Forum of the American Helicopter Society, Phoenix, AZ, May 9-11 2006.

[5] Ribera, M., and Celi, R., "Time Marching Simulation Modeling in Descending Flight Through the Vortex Ring State," Proceedings of the 63rd Annual Forum of the American Helicopter Society, Virginia Beach, VA, May 1 - 3, 2007 2007.

[6] Theodore, C., and Celi, R., "Helicopter Flight Dynamic Simulation with Refined Aerodynamic and Flexible Blade Modeling," *Journal of Aircraft*, Vol. 39, No. 4, July-August 2002, pp. 577–586.

[7] Micallef, D., van Bussel, G., Ferreira, C., and Sant, T., "An investigation of radial velocities for a horizontal axis wind turbine in axial and yawed flows," *Wind energy journal*, 2012.

[8] Bhagwat, M. J., and Leishman, J. G., "Stability, Consistency and Convergence of Time Marching Free-Vortex Rotor Wake Algorithms of Time-Marching Free-Vortex Rotor Wake Algorithms," *Journal of the American Helicopter Society*, Vol. 46, No. 1, January 2001, pp. 59–71.

[9] Ananthan, S., and Leishman, J. G., "Role of Filament Strain in the FreeVortex Modeling of Rotor Wakes," *Journal of the American Helicopter Society*, Vol. 49, No. 2, Apr. 2004, pp. 176–191.

[10] Powell, M. J. D., *A Hybrid Method for Nonlinear Equations. Numerical Methods for Nonlinear Algebraic Equations* Gordon and Breach, 1970.

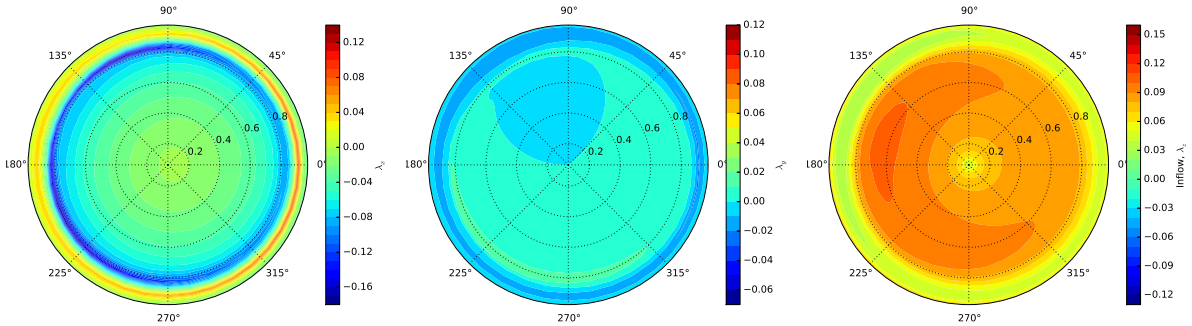

(a) λ_x, 1kt (b) λ_y, 1kt (c) λ_z, 1kt

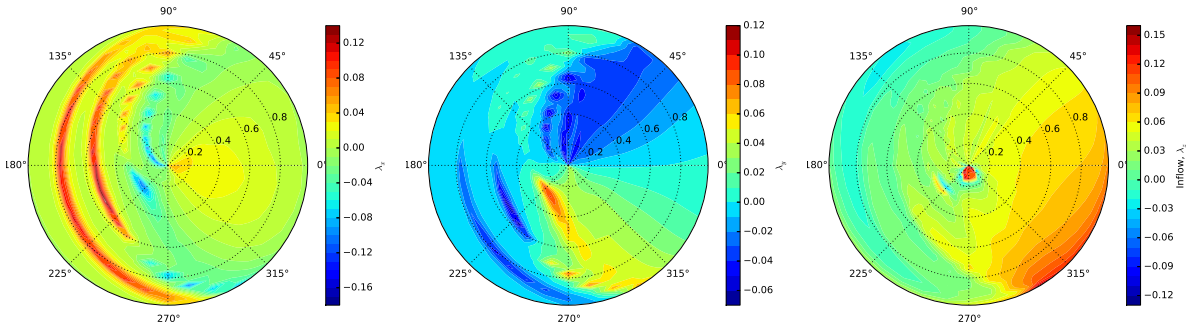

(d) λ_x, 60kt (e) λ_y, 60kt (f) λ_z, 60kt

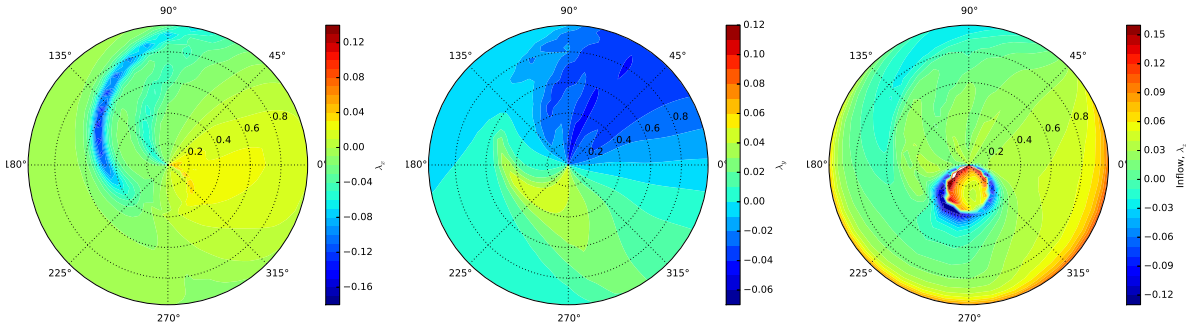

(g) λ_x, 140kt (h) λ_y, 140kt (i) λ_z, 140kt

Figure 1: x, y and z components of the induced velocities at 1 kt, 60 kts and 140 kts.

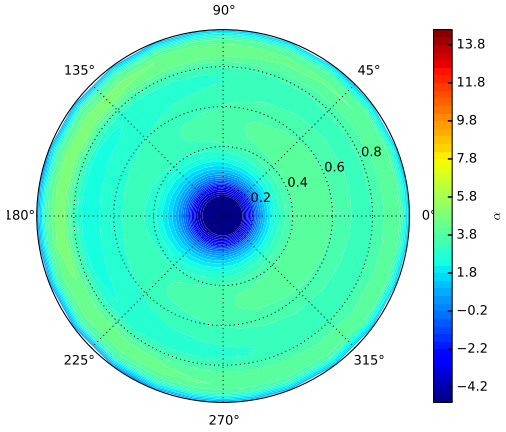

(a) α, $\lambda_x = \lambda_y = 0$, 1kt

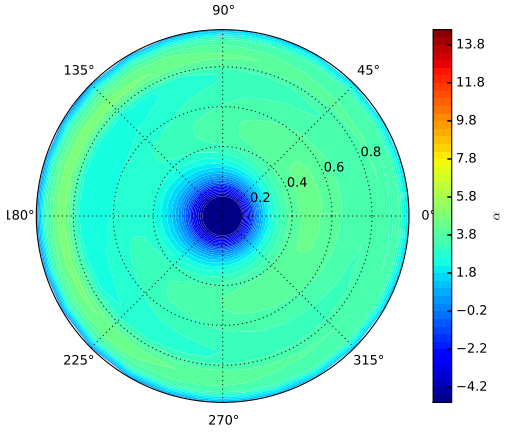

(b) α, 1kt

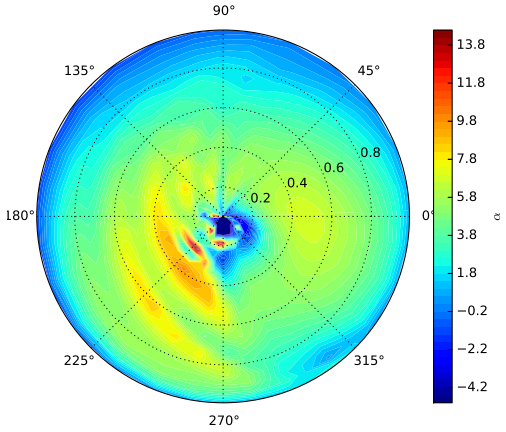

(c) α, $\lambda_x = \lambda_y = 0$, 60kt

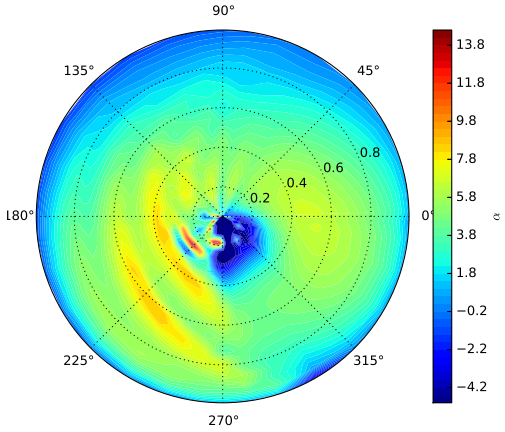

(d) α, 60kt

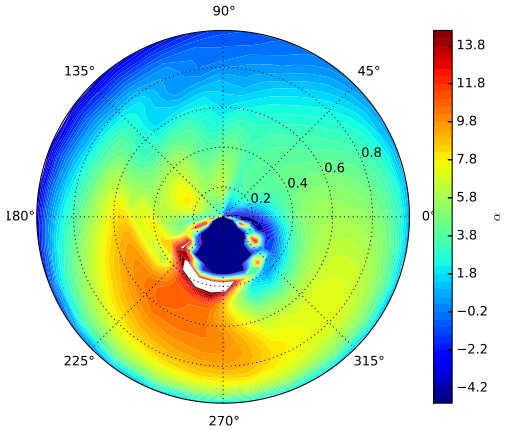

(e) α, $\lambda_x = \lambda_y = 0$, 140kt

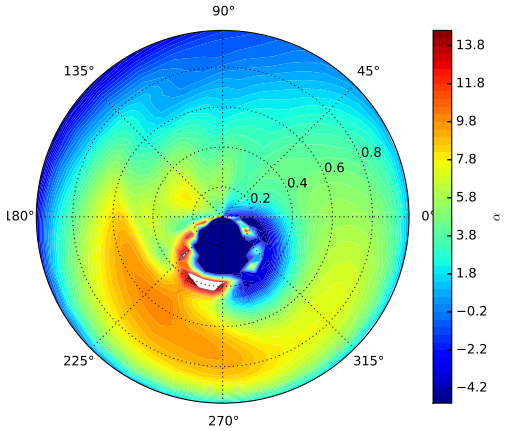

(f) α, 140kt

Figure 2: Angle of attack α at 1 kt, 60 kts and 140 kts, without and with the x and y induced velocities.

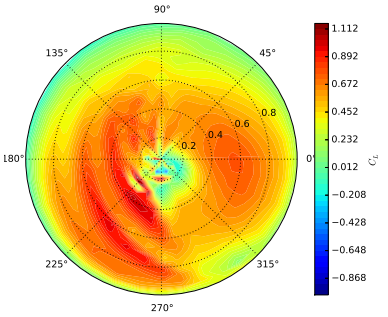

(a) C_L, $\lambda_x = \lambda_y = 0$, 60kt

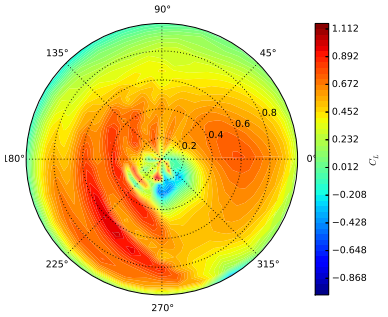

(b) C_L, 60kt

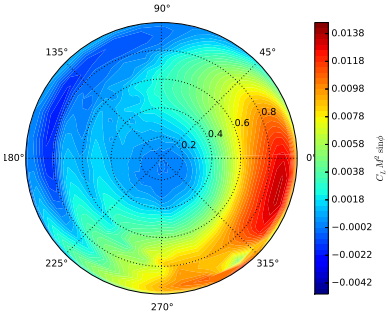

(c) $rC_L M^2 \sin\phi$, $\lambda_x = \lambda_y = 0$, 60kt

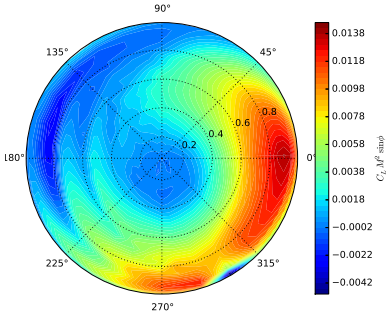

(d) $rC_L M^2 \sin\phi$, 60kt

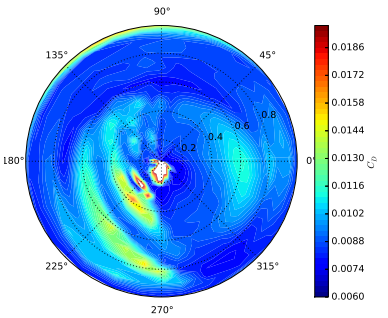

(e) C_D, $\lambda_x = \lambda_y = 0$, 60kt

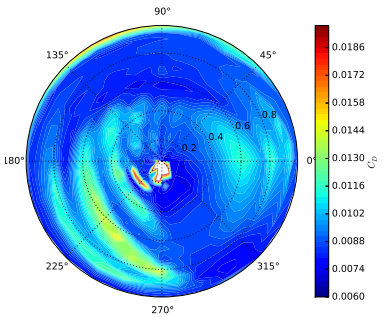

(f) C_D, 60kt

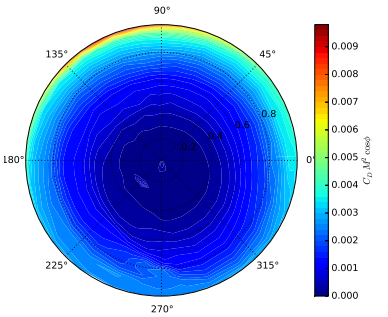

(g) $rC_D M^2 \cos\phi$, $\lambda_x = \lambda_y = 0$, 60kt

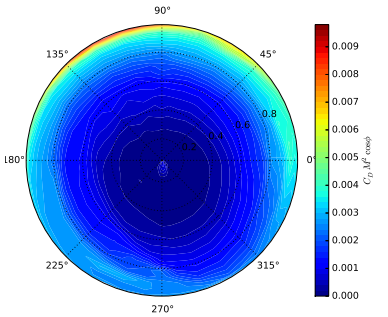

(h) $rC_D M^2 \cos\phi$, 60kt

Figure 3: Lift and Drag coefficients, C_L and C_D, and elemental induced and profile torque, $rC_L M^2 \sin\phi$ and $rC_D M^2 \cos\phi$, at 1 kt, 60 kts and 140 kts, without and with the x and y induced velocities.

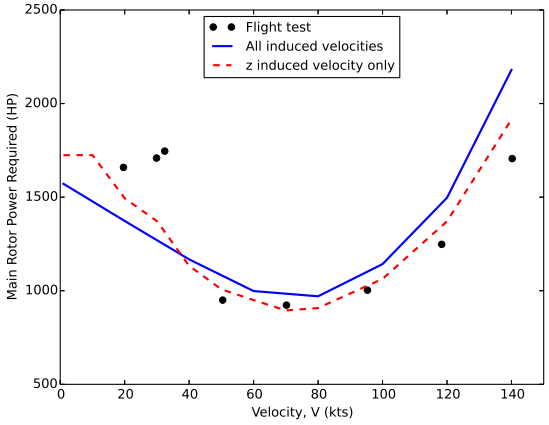

Figure 4: Power as a function of speed, in HP.

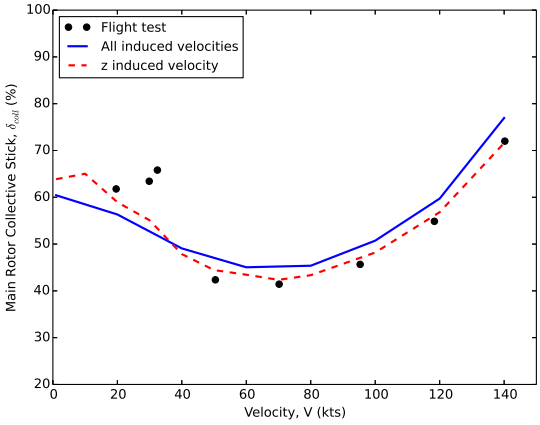

Figure 7: Collective as a function of speed, in $\%$.

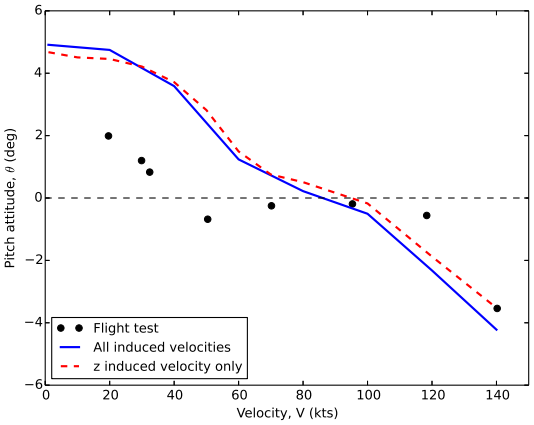

Figure 5: Pitch attitude as a function of speed, in degrees.

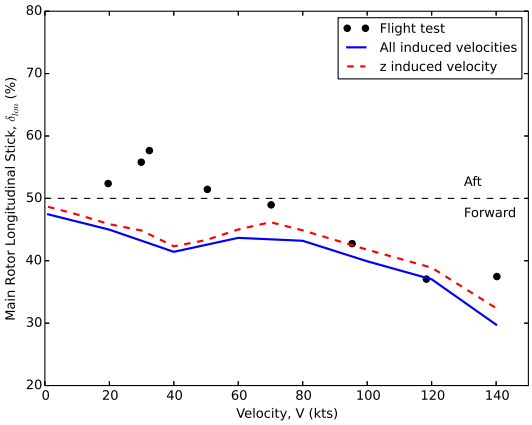

Figure 8: Longitudinal stick displacement as a function of speed, in$\%$.

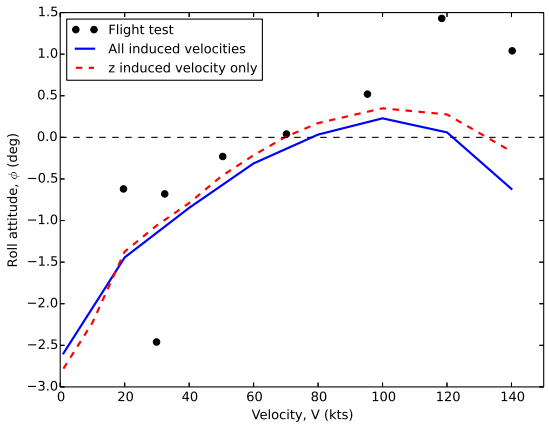

Figure 6: Bank angle as a function of speed, in degrees.

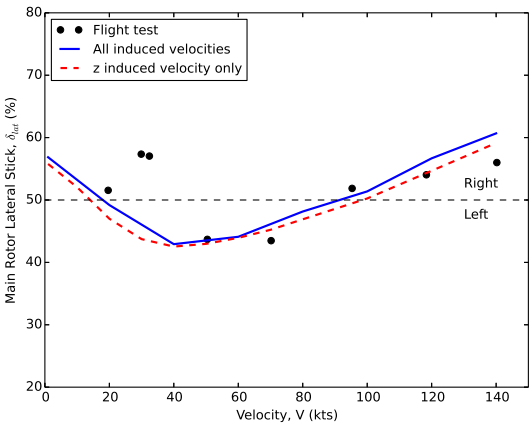

Figure 9: Lateral stick displacement as a function of speed, in $\%$.

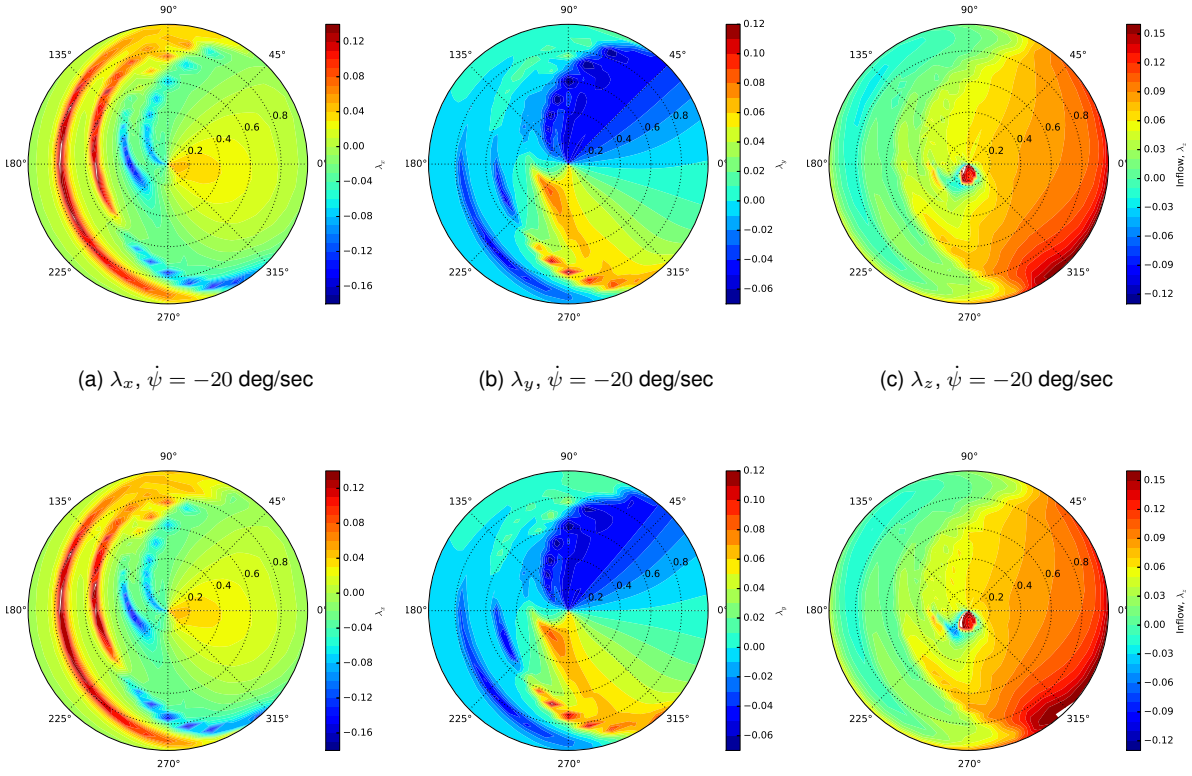

(a) λ_x, $\dot{\psi} = -20$ deg/sec (b) λ_y, $\dot{\psi} = -20$ deg/sec (c) λ_z, $\dot{\psi} = -20$ deg/sec

(d) λ_x, $\dot{\psi} = 20$ deg/sec (e) λ_y, $\dot{\psi} = 20$ deg/sec (f) λ_z, $\dot{\psi} = 20$ deg/sec

Figure 10: x, y and z components of the induced velocities at 60 kts and turn rates of -20 deg/sec and 20 deg/sec.

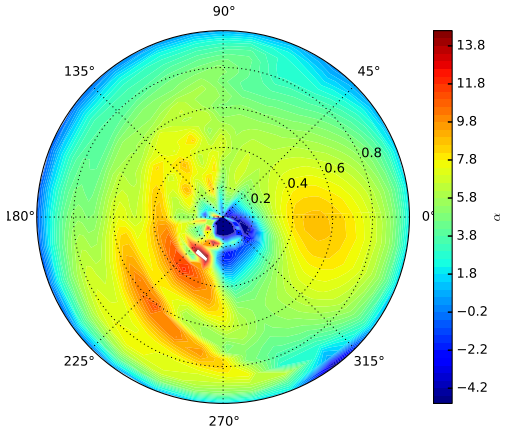

(a) α, $\lambda_x = \lambda_y = 0$, $\dot{\psi} = -20$ deg/sec

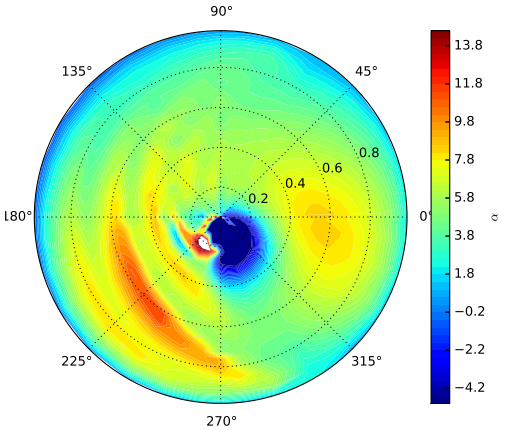

(b) α, $\dot{\psi} = -20$ deg/sec

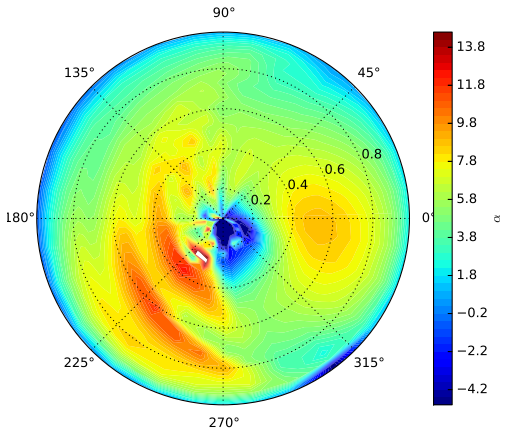

(c) α, $\lambda_x = \lambda_y = 0$, $\dot{\psi} = 20$ deg/sec

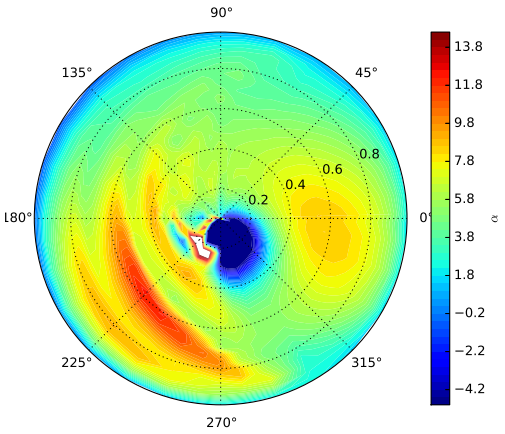

(d) α, $\dot{\psi} = 20$ deg/sec

Figure 11: Angle of attack α at 60 kts, for turn rates of 20 deg/sec and 20 deg/sec without (left) and with (right) the x and y induced velocities.

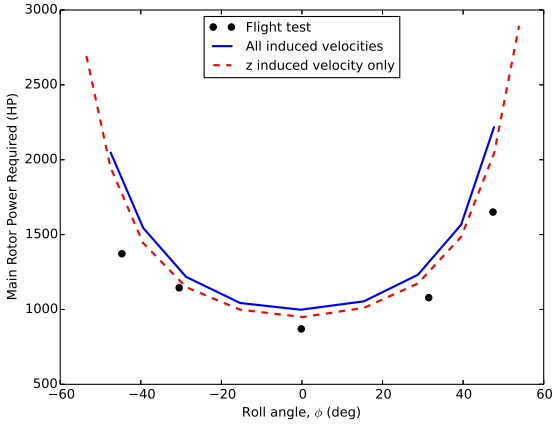

Figure 12: Power as a function of roll angle, ϕ, in HP.

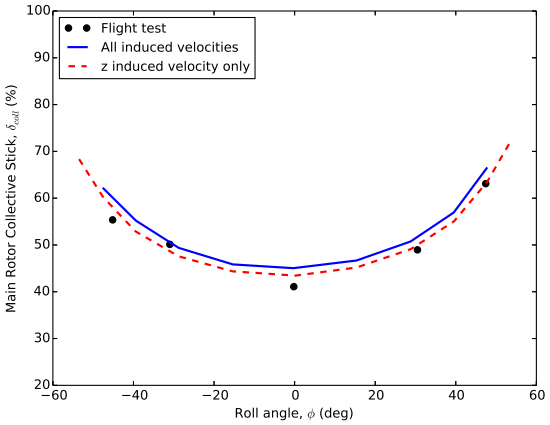

Figure 15: Main rotor collective as a function of roll angle, ϕ, in $\%$.

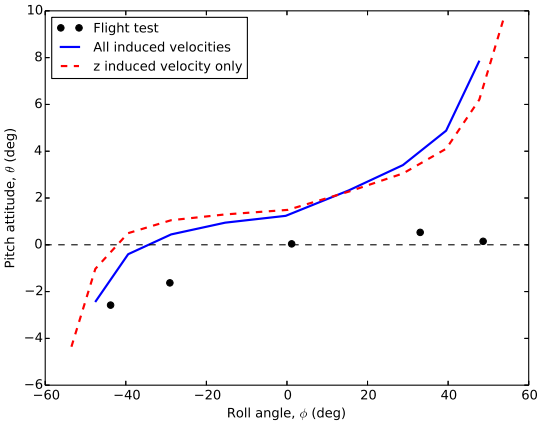

Figure 13: Pitch attitude as a function of roll angle, ϕ, in degrees.

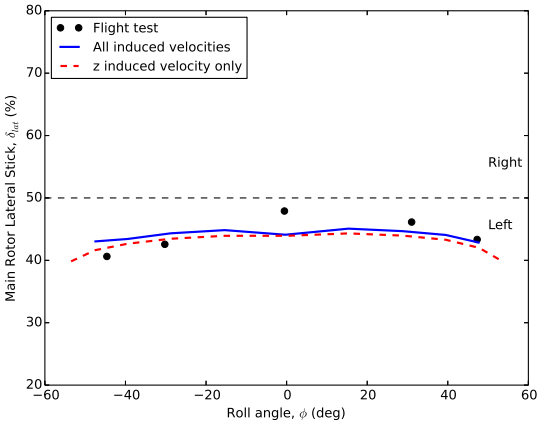

Figure 16: Lateral stick displacement as a function of roll angle, ϕ, in $\%$.

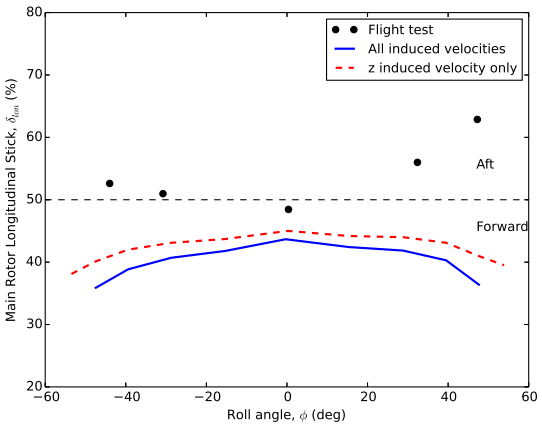

Figure 14: Longitudinal stick displacement as a function of roll angle, ϕ, in $\%$.

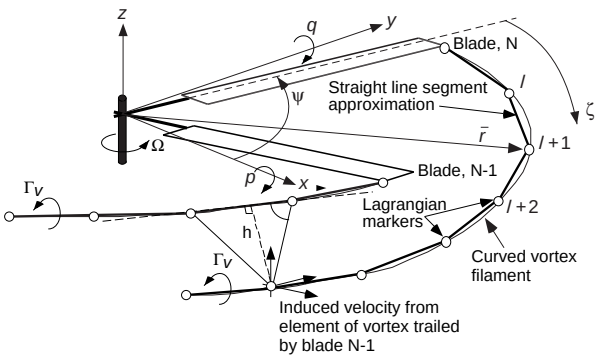

Figure 17: Free wake discretisation in the azimuth (ψ) and filament (ζ) directions.